Acta Materialia 249 (2023) 118816

Contents lists available at ScienceDirect

Acta Materialia

journal homepage: www.elsevier.com/locate/actamat

Fe segregation as a tool to enhance electrical conductivity of grain boundaries in Ti(Co,Fe)Sb half Heusler thermoelectrics

Ruben Bueno Villoro [a,*], Maxwell Wood [b], Ting Luo [a], Hanna Bishara [a], Lamya Abdellaoui [a], Duncan Zavanelli [b], Baptiste Gault [a,c], Gerald Jeffrey Snyder [b], Christina Scheu [a,*], Siyuan Zhang [a,*]

[a] Max–Planck-Institut für Eisenforschung GmbH, Max–Planck-Straße 1, 40237, Düsseldorf, Germany
[b] Northwestern University, Clark Street 633, 60208, Evanston, USA
[c] Department of Materials, Royal School of Mines, Imperial College London, Prince Consort Road, London SW7 2BP, UK

ARTICLE INFO

Keywords:
Grain boundaries
Half Heusler intermetallics
Thermoelectrics
Characterization
Electrical conductivity

ABSTRACT

Complex microstructures are found in many thermoelectric materials and can be used to optimize their transport properties. Grain boundaries in particular scatter phonons, but they often impede charge carrier transfer at the same time. Designing grain boundaries in order to offer a conductive path for electrons is a substantial opportunity to optimize thermoelectrics. Here, we demonstrate in TiCoSb half Heusler compounds that Fe-dopants segregate to grain boundaries and simultaneously increase the electrical conductivity and reduce the thermal conductivity. To explain these phenomena, three samples with different grain sizes are synthesized and a model is developed to relate the electrical conductivity with the area fraction of grain boundaries. The electrical conductivity of grain interior and grain boundaries is calculated and the atomic structure of grain boundaries is studied in detail. Segregation engineering in fine-grained thermoelectrics is proposed as a new design tool to optimize transport properties while achieving a lower thermal conductivity.

1. Introduction

Thermoelectric materials convert thermal gradients into electricity and vice versa, as applied in solid state electricity generators and Peltier coolers respectively [1,2]. Efficiency in thermoelectrics is characterized by the figure of merit zT (Eq. (1)):

$$zT = \sigma S^2 T/\kappa \quad (1)$$

Where σ is the electrical conductivity, S the Seebeck coefficient, T the temperature and κ the thermal conductivity.

Efficiency of thermoelectric materials can be affected by microstructural features such as grain boundaries (GBs) as they reduce thermal conductivity by phonon scattering [3–5], but this is usually accompanied by a reduction in the electrical conductivity [6–10]. Some examples of the negative effect of GBs on the electrical conductivity in thermoelectrics are reported in literature [11–17]. In Mg_3Sb_2–Mg_3Bi_2 alloys, a reduction of σ at room temperature of 2-3 times is observed by reducing the grain size [16]. In $(Hf_{0.3}Zr_{0.7})_{0.94}Nb_{0.06}CoSb$ a reduction from 9.2 to 4.0 × 10^4 S m^{-1} at room temperature is observed by reducing the grain size [18].

In metals, GB resistivity can be mitigated by introducing doping elements. For example, Zn, Cd, and Be segregations at Σ13b and Σ17a GBs in Cu have been found to reduce the GB resistivity compared to their counterparts of pure Cu, which is caused by a reduction of empty states at the GBs [19]. In semiconducting thermoelectrics, the loss of conductivity at GBs has been partially counteracted in $NbCo_{1-x}Pt_xSn$ using Pt segregation [20] and in Ti doped NbFeSb [21]. Conductivity of polycrystalline materials can be increased due to the presence of GB complexions and low angle GBs [22–24]. Therefore, GB engineering [25], including segregation engineering [26,19], could lead to more conductive GBs. Recent results on Cu_2SnS_3 semiconductors show that a reduction of grain size can increase electrical conductivity and overall efficiency [27]. Density functional theory was used to simulate different possible atomic arrangements at GBs and its implications on the band gap, concluding that some atomic arrangements reduce the band gap of GBs close to zero [27].

In recent years, half Heusler alloys have attracted interest as mid to high temperature thermoelectrics [28] for energy harvesting [29,30], including automotive waste heat recovery [31]. Half Heusler alloys are composed of three elements in 1:1:1 stoichiometry (XYZ) where each element occupies a different crystallographic site in the $F\bar{4}3m$ space group. There is a wide design space from the choice of X,Y and Z to substitutional doping on the three sites making the properties (such as the band gap) highly tunable [32]. In metallurgy, many multinary

* Corresponding authors.
E-mail addresses: r.bueno@mpie.de (R. Bueno Villoro), c.scheu@mpie.de (C. Scheu), siyuan.zhang@mpie.de (S. Zhang).

https://doi.org/10.1016/j.actamat.2023.118816
Received 8 June 2022; Received in revised form 23 January 2023; Accepted 26 February 2023
Available online 2 March 2023

alloy systems are known to cause segregation or depletion at GBs, which could either inhibit grain growth [33,34,26,35] or promote abnormal grain growth [36,37]. Applying the same design principle to half Heusler intermetallics, there is an exciting opportunity to explore nanocrystalline systems with dopants to tune the GB conductivity and control grain growth. Fe-doped TiCoSb half Heusler exhibits Fe segregation at GBs [38] and a moderate zT up to 0.4 at 850 K for the composition $TiCo_{0.7}Fe_{0.3}Sb$ [39]. Therefore, this material is a good candidate for investigation of GB segregation and its relationship with transport properties.

In this work, we present a microstructure-properties correlative study where GBs in $TiCo_{0.7}Fe_{0.3}Sb$ are demonstrated to improve the electrical conductivity and simultaneously reduce the thermal conductivity, both important to optimize the zT. High resolution scanning transmission electron microscopy (STEM), energy dispersive X-ray spectroscopy (EDX) and atom probe tomography (APT) enabled us to perform a detailed study of the chemistry and atomic arrangement of the GBs down to the atomic scale. We attributed Fe segregation and Co depletion at the GBs to the electrically more conductive GBs than the bulk. Thus far, theory has been developed to account for the effect of more resistive GBs on the overall electrical conductivity [15]. Here, we develop a two-phase model as a theoretical framework to quantify the effect of more conductive GBs into the overall electrical conductivity.

2. Experimental

2.1. Sample preparation

The $Ti(Co_{0.7}Fe_{0.3})Sb$ samples have been produced using stoichiometric ratios of bulk Ti slugs (99.99% Sigma-Aldrich), Fe lumps (99.99% Alpha Aesar), Co slugs (99.99% Alpha Aesar), and Sb shot (99.999% Alpha Aesar). Starting elements were cut into small pieces and loaded into an Edmund-Buehler MAM-1 arc melter where they were melted together 5 times flipping in between each melt. The arc melted button was then pulverized using a stainless-steel vial for one hour using a SPEX sample prep 800 series mixer/mill. This powder was consolidated using an induction heated rapid hot-press under a flowing argon atmosphere within a 12.7 mm diameter high-density graphite die. The samples were then pressed at 1173, 1373 or 1473 K for one hour at 45 MPa. Once pressed, the samples were polished to remove excess graphite from its surface, sealed in an evacuated fused silica ampule, and annealed at 900 K for one week.

2.2. Properties characterization

Electronic transport measurements were conducted on disks of approx. 2 mm thickness and approx. 13 mm of diameter under dynamic high vacuum up to 875 K with a ramp speed of 75 K h^{-1}. Resistivity and Hall coefficient were measured concurrently using the van der Pauw technique with pressure-assisted molybdenum contacts equipped with a 2 T magnet. Resistivity was measured also in a LINKAM - HFS600 probing system with 4 tungsten needles supported by springs. Temperature was increased in steps of 50 K at a rate of 5 K min^{-1} and 5 min stabilization were given at each temperature, which was proven sufficient to reach thermal equilibrium by repeating 100 direct current pulse measurements. Both measurement instruments provided results of comparable magnitude.

Thermal diffusivity measurements were taken with a Netzch LFA 457 under purged flowing argon up to 875 K with a ramp speed of 75 K h^{-1}. Thermal conductivity was calculated estimating heat capacity with the Dulong-Petit law. Seebeck coefficient was measured under dynamic high vacuum up to 875 K with a home built system using Chromel-Nb thermocouples.

2.3. Microstructure characterization

Solid X-ray diffraction (XRD) was performed on polished surfaces using a diffractometer D8 advance A25-X1 with a Co K_α source (λ = 0.178897 nm).

Samples for SEM investigation were grinded using SiC papers and polished using diamond and OPS suspension solutions. SEM characterization was done in a Sigma 500 Zeiss microscope. Electron back-scatter diffraction (EBSD) was performed at 15 kV, 15 nA and a working distance of 20 mm using a EDAX/TSL system with a Hikari camera.

TEM sample preparation was done using a Thermo scientific SCIOS2 focused-ion beam with a 30 kV Ga^+ beam to prepare a lamella and thinning to < 150 nm. Final thinning and cleaning was done at 5 and 2 kV. A general procedure similar to the one described by Schaffer et al. [40] has been used.

The STEM-EDX characterization was performed on a Titan Themis image-corrected instrument operated at 300 kV with a four-quadrant silicon-drift detector (Super-X). STEM-EDX spectrum imaging was acquired using approx. 25 min acquisition time for each map, 5 maps per sample and each map covering an area of 20 nm × 20 nm. Multivariate analysis was performed for noise reduction [41] and the Cliff–Lorimer formula was used for elemental quantification.

Atomic resolution STEM imaging experiments were performed on a Titan Themis probe-corrected instrument with a collection semiangle of 24 mrad and aprox. 0.1 nm probe size equipped with a high angle annular dark field (HAADF) detector with a collection angle between 73 and 200 mrad.

STEM-electron energy loss spectroscopy (EELS) spectrum imaging was obtained using a Gatan Quantum ERS energy filter in image-coupled mode with a entrance aperture of 35 mrad.

Needle-shaped APT specimens were prepared using a Helios 600i dual-beam focused-ion beam, following the procedures described by Thompson et al. [42]. A Cameca LEAP 5000XR system was used in the laser mode. The base temperature of the specimen was kept at 50 K. The laser energy was 30–35 pJ and the pulse frequency was 125 kHz. Cameca IVAS 3.8.8 was used to reconstruct and analyze the APT data.

3. Results and discussion

3.1. Crystal structure and grain size

Three samples with $TiCo_{0.7}Fe_{0.3}Sb$ nominal composition and different grain sizes were obtained by arc melting, ball milling, hot pressing and annealing. By changing the hot pressing temperature to 1173, 1373 and 1473 K, the grain size of the samples was systematically modified. The three samples are referred to as HP-1173K, HP-1373K and HP-1473K respectively within this work. XRD confirms that all three samples have a single half-Heusler phase (Supplemental Fig. 1). Lattice parameters obtained averaging the values from all XRD peaks (2-sigma uncertainty) are 590.0 ± 1.0 pm, 590.3 ± 0.8 pm and 590.0 ± 0.6 pm for HP-1173K, HP-1373K and HP-1473K respectively. The three samples do not show a difference in strains, and their lattice parameters are in close agreement with the value of 589.3 pm reported by Wu et al. for the same composition [39]. Peak splitting is observed due to the emission of Co-$K_{\alpha 2}$ X-rays by the source.

EBSD mapping was performed to study the characteristics of grains and GBs in the samples. Fig. 1 present the EBSD maps of HP-1173K(a), HP-1373K(b) and HP-1473K(c) with the [001] inverse pole figure shown in the inset. HP-1173K has the finest grain size of 0.26 μm, HP-1373K an intermediate grain size of 0.42 μm, and HP-1473K the biggest grain size of 5 μm. Supplemental Fig. 2 shows (a) the grain diameter distribution versus area fraction from the EBSD data as well as (b) the GB misorientation angle vs number fraction, confirming a random (Mackenzie) distribution of GBs for all three samples [43].

EBSD maps reveal that some grains contain subgrains, i.e., low angle GBs. Low angle GBs are composed by arrays of dislocations at

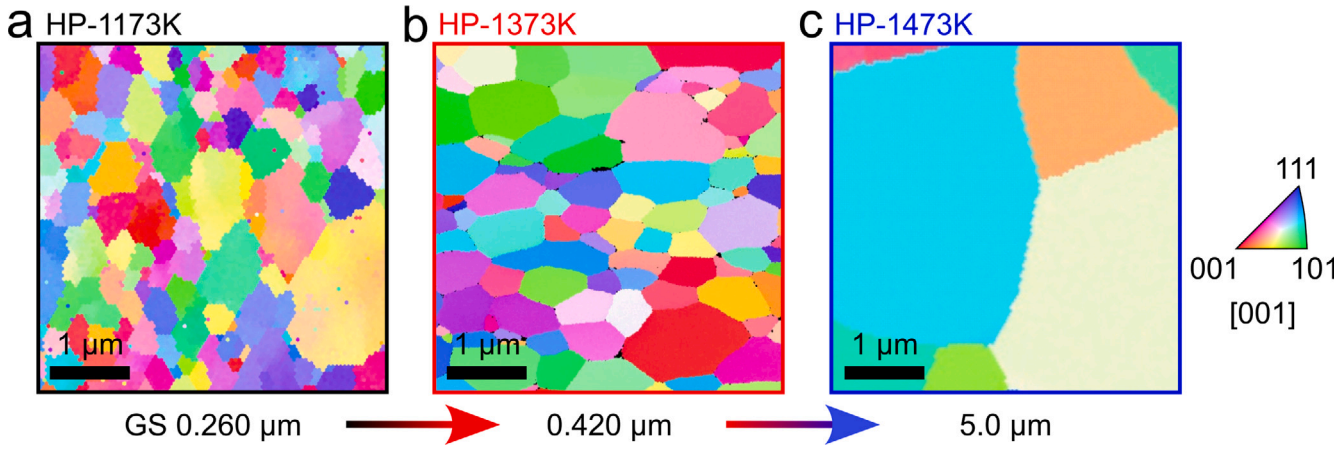

Fig. 1. Grain size changes with hot pressing temperature. EBSD maps of (a) HP-1173K, (b) HP-1373K and (c) HP-1473K.

periodic spacing [44], which are known to reduce the thermal conductivity [45,46] and the electrical conductivity [47]. The black features observed in the EBSD and SEM micrographs shown later in this work are mainly pores originated from consolidating ball milled powder, which have not been completely eliminated during sintering [48]. The theoretical density of the material is calculated from the lattice parameters obtained by XRD as 58.40 ± 0.08 atoms nm^{-3} or 7.36 ± 0.01 g cm^{-3}. The experimental density of the samples is 98% for HP-1173K and 97% for HP-1373K relative to the theoretical value. Therefore, a volume fraction of 2%–3% of pores is expected for all samples. Small amounts of TiO_x particles were found by STEM-EDX (Supplemental Fig. 3) and EELS (Supplemental Fig. 4), which have no major effect on the properties due to the low volume content.

From the micrometer-scale characterization, the three samples only differ in their grain sizes. Therefore, the changes observed in the properties across samples can be attributed to the changes in the grain size and potentially to nanometer-scale features, as discussed later in this work.

3.2. Electrical conductivity

In order to understand the role of the grain size in the bulk properties, the electrical conductivity was measured between 298 and 773 K using the van der Pauw technique [49]. SEM micrographs of the three samples are presented in Fig. 2a–c where the grain size can be observed. The electrical conductivity vs T of all samples is presented in Fig. 2d. At room temperature, electrical conductivity (σ) increases from 240 to 348 S cm^{-1} as the grain size decreases from 5 μm to 0.26 μm. Therefore, it is derived that more GBs in $TiCo_{0.7}Fe_{0.3}Sb$ lead to an increase of the bulk electrical conductivity. In order to understand this phenomenon, we model GBs as a phase with different properties with respect to the bulk phase [15].

The standard two phase model used for resistive GBs is based on the idea of the brick layer model [15]. In such visualization, there are conductive grains (bricks) and resistive GBs (the mortar). There are two major options for conductive paths, the first is through the grains, interrupted by GBs and the second is purely through the GBs. If the boundaries are more resistive than the grain, the second path can be neglected for conduction. Then the effective circuit becomes a grain in series with a GB. Hence the total resistivity is the sum of the grain and GB resistivity. However, for conductive GBs, the second path should not be neglected. Instead, the circuit becomes a parallel circuit. On one branch there is just the GB, and on the other branch there is the grain and GB resistivity in series. If the GB conductivity is higher than the grain interior, the GB and grain in series approximates to just the grain resistivity. This gives a different model for conductive GBs where the total conductivity is the sum of the conductivity of individual phases.

A simple model is developed (Eq. (2)) to estimate the contribution of grains and GBs to the total electrical conductivity where GBs serve as a fast conduction path for electrons. The electrical conductivity is given by:

$$\sigma_{total} = \sigma_G f_G + \sigma_{GB} f_{GB} \tag{2}$$

Where σ_{total} is the measured electrical conductivity, σ_G and σ_{GB} are the electrical conductivity of the grain interior and GBs, respectively, and f_G and f_{GB} are their respective 2D-projected area fractions.

Since $f_G = 1 - f_{GB}$, Eq. (2) can be reformulated to Eq. (3):

$$\sigma_{total} = \sigma_G + f_{GB}(\sigma_{GB} - \sigma_G) \tag{3}$$

And f_{GB} for a hexagonal grid of grains is calculated as shown in Eq. (4):

$$f_{GB} = 1 - \left(\frac{g-d}{g}\right)^2 \tag{4}$$

where d is the thickness of the GB and g is the grain size (grain interior plus thickness of GB). d = 4 nm is chosen in accordance with the APT data presented later in this work. The calculation of f_{GB} is explained in more detail in the supplemental information and Supplemental Fig. 6.

By doing a linear regression of Eq. (3), the contributions of σ_G and σ_{GB} to σ_{total} at all temperatures are obtained and plotted in Fig. 2e. A clear linear correlation between σ_{total} and f_{GB} at room temperature is shown in Fig. 2f. Since f_{GB} is relatively close to 0 for HP-1473K, the influence of GBs in this sample is minimal. As a result, the increase of σ_G with temperature follows the same trend as the measurements on HP-1473K. At room temperature, the value obtained from the linear regression of σ_G = 239 ± 1 S cm^{-1} is very close to σ_{total} = 240 S cm^{-1} measured on this sample and very similar to the measurement of Wu et al. [39] on the same material of σ = 242 S cm^{-1}. We assume that they studied a sample where the effect of GBs was negligible.

The increased conductivity in the other samples can be attributed to their increasing f_{GB}. The value obtained from the linear regression at room temperature for σ_{GB} is 3.3 ± 0.1 × 10^3 S cm^{-1}. σ_{GB} is more than one order of magnitude higher than σ_G, thus, GBs will act as a conductive path for electrons. A schematic of the electron pathway is shown in Fig. 2g where the grains are represented by hexagons and GBs by black lines. As GBs are the more conductive phase, charge carriers are preferentially conducted through the GB (yellow path) while the path inside the grains is more resistive (blue lines).

As shown in the σ_{GB} vs d plot in Supplemental Fig. 5, the magnitude of σ_{GB} varies from 4.4 × 10^3 S cm^{-1} for d = 3 nm to 2.6 × 10^3 S cm^{-1} for d = 5 nm at room temperature. Then, magnitude of σ_{GB} varies up to 33% within the considered range of d.

Carrier concentrations were measured at room temperature, 3.1·10^{20} cm^{-3} for HP-1173K and 2.7·10^{20} cm^{-3} for HP-1373K. Their

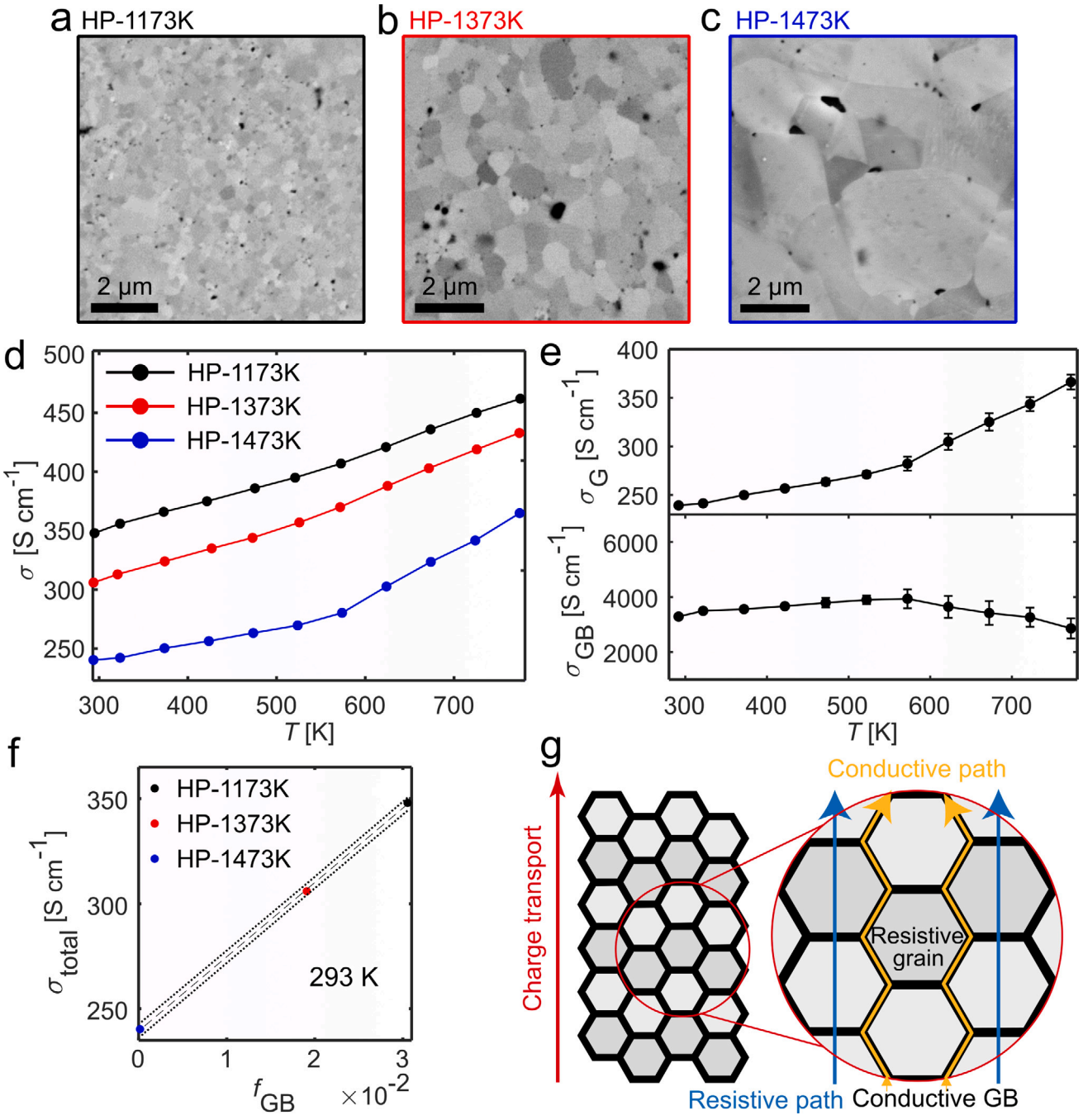

Fig. 2. SEM images of (a) HP-1173K, (b) HP-1373K and (c) HP-1473K. (d) Electrical conductivity vs temperature plots for HP-1173K (black), HP-1373K (red) and HP-1473K (blue). (e) Contributions of grain (σ_G) and GB (σ_{GB}) to the total electrical conductivity vs temperature. (f) Electrical conductivity at room temperature vs area fraction of grain and linear regression (black dashed line) and (g) scheme of the electron pathways through the GBs. (For interpretation of the references to color in this figure legend, the reader is referred to the web version of this article.)

effective masses [50,51] were hence calculated as $2.1m_e$ and $2.5m_e$, respectively, where m_e is the mass of an electron. The weighted mobility (μ_w) is calculated [52] and shown in Supplemental Fig. 12. The μ_w vs T curve is fitted to a power function, with the exponents of $T^{-0.74}$ for HP-1173K and $T^{-0.60}$ for HP-1373K. The weighted mobility results further confirm that the major scattering mechanism for charge carriers is not by acoustic phonons ($T^{-1.5}$), but closer to ionized impurity ($T^{-0.5}$) [53].

Seebeck coefficient (Supplemental Fig. 7a) and electrical conductivity (Fig. 2d) increase with temperature. These results suggest that minority carrier concentration is significant enough to affect carrier concentration and Seebeck measurements.

We believe the GB are metallic due to the observed change and properties and observed composition, thus we do not expect the grain boundary material alone to be a good TE material. As the carrier concentration increases for HP-1173K, the Seebeck coefficient decreases (supplemental Fig. 7a, 13% reduction with respect to HP-1373K at room temperature). This also leads to a reduction in the power factor (supplemental Fig. 7b), which suggests that the Seebeck coefficient and the electrical conductivity are still coupled. Nevertheless, we notice that HP-1173K maintains similar zT (Supplemental Fig. 7d) values to HP-1373K, as the thermal conductivity (κ) decreases from 4.7 W m^{-1} K^{-1} for HP-1373K to 4.2 W m^{-1} K^{-1} for HP-1173K at 323 K (Supplemental

Fig. 7c). By using the Wiedemann–Franz law (Eq. (5)), the electronic contribution to κ is calculated (Supplemental Fig. 7e) and the lattice thermal conductivity is obtained (Supplemental Fig. 7f).

$$\kappa = \kappa_e + \kappa_l = L\sigma T + \kappa_l \quad (5)$$

where κ_e is the electronic thermal conductivity, κ_l is the lattice thermal conductivity and L is the Lorenz factor calculated from the experimental Seebeck measurements following the procedure of Snyder et al. [54], which varies from 1.76 to 1.93 × 10^{-8} WΩK^{-2}.

Thermal conductivity occurs mainly at the grain interior, therefore, σ_G can be used instead of σ_{total} to calculate κ_e [15]. When σ_G is used, κ_e is further reduced from 0.22 to 0.15 W m^{-1} K^{-1} at 323 K in HP-1173K. Accordingly κ_l increases by 0.06 W m^{-1} K^{-1} at 323 K and 0.12 W m^{-1} K^{-1} at 823 K on HP-1173K. The effect on κ_l and κ_e of using the calculated L instead of the free electron value and using σ_G instead of σ_{total} is shown for all temperatures in Supplemental Fig. 8.

The reduction of κ in fine-grained materials is well documented in thermoelectrics [55,56,15]. This can be attributed to phonon scattering by GBs [57,5].

Thus far, we have demonstrated GBs to simultaneously increase the electrical conductivity and reduce the thermal conductivity of fine-grained $TiCo_{0.7}Fe_{0.3}Sb$. Overall efficiency is similar for HP-1173K and HP-1373K (Supplemental Fig. 7d) at temperatures below 600 K. At higher temperatures, HP-1373K has higher zT mainly due to an increased Seebeck coefficient.

3.3. Chemistry of GBs

To understand the origin of the unusual conductive behavior of the GBs, the chemistry of the GBs is studied at the nanoscale using APT and STEM-EDX. Fig. 3a shows a schematic including the viewing directions and specimen sizes for the SEM, STEM and APT experiments. On the TEM lamella, the size of an EDX map is indicated with a purple square. The analyzed volume with STEM is on the order of 2 μm^3 and for APT, 0.02 μm^3. Therefore, both techniques are complementary since STEM allows the investigation of a larger volume to obtain more statistics on the GB composition by EDX, while APT enables more precise measurements on the chemistry in 3D [58] in much smaller volumes.

Fig. 3b presents the EDX maps of a GB where Fe segregation and Co depletion are clearly visible. Gibbsian interfacial excess (Γ) was used to quantify the excess of atoms at the GB per unit area with respect to the matrix [59]. This approach enables the quantification and comparison of the magnitude of the segregation across all GBs, regardless of their orientation, faceting, curvature, or any other effect that spreads and broadens the analytical signal. We used the approach outlined by Maugis and Hoummada to calculate the excess since atomic concentration is comparable at both grains [60]. A constant sample density of 58.40 atoms nm^{-3} is applied to convert the atomic compositions (in at.%) into concentrations (in atoms nm^{-3}). The obtained values of Γ are summarized in Table 1 and Fig. 3c. The average matrix concentration values (in atoms nm^{-2}) for STEM-EDX and APT are shown in Supplemental table 1 and present little differences.

Table 1
Γ values in atoms nm^{-2}, positive and negative values represent segregation and depletion, respectively.

Technique	Sample	Ti	Co	Fe	Sb
STEM-EDX	HP-1173K	1.0 ± 2.0	−11.9 ± 1.8	8.9 ± 1.1	2.5 ± 1.8
STEM-EDX	HP-1373K	2.4 ± 3.2	−11.4 ± 5.0	7.1 ± 2.7	1.9 ± 3.7
STEM-EDX	HP-1473K	−1.3 ± 1.7	−9.6 ± 4.9	9.8 ± 4.1	1.1 ± 0.6
APT	HP-1173K	−0.8 ± 1.5	−10.7 ± 3.0	9.7 ± 2.6	0.9 ± 2.3
APT	HP-1373K	−1.7 ± 7.6	−8.5 ± 0.8	7.9 ± 0.4	−1.3 ± 1.8

The Gibbsian interfacial excess obtained by APT and STEM-EDX shows a comparable magnitude. Within GBs of the same sample, dispersion of results is observed for both STEM and APT data, and the distributions are represented by the error bars (1-sigma). Some segregation and depletion of both Ti and Sb are observed in the APT and EDX data but their segregation behavior is uncertain since Γ has smaller magnitude than their statistical variance. On the other hand, all samples present Fe segregation and Co depletion of comparable magnitudes with statistical significance.

In order to model the electronic properties, GBs in all samples are approximated as one phase with the same electrical conductivity. This is a reasonable approximation as the average Γ is similar for all samples (Fig. 3c). Although the segregation behavior may depend on the geometry of individual GBs (hence the statistical dispersion), the same distribution of GBs (supplemental Fig. 2b) makes the statistical ensembles for all three samples alike, making the modeled σ_{GB} the average values for the ensembles.

Fig. 3d presents an APT 3D reconstruction obtained from HP-1373K (Additional APT data is shown in supplemental figures 9,10 for HP-1173K in supplemental Fig. 11 for HP-1373K.). Fe segregation is readily visible across three GBs forming a triple junction. A line composition profile is obtained from the black cylinder visible in the APT reconstruction, enabling quantification of the Fe segregation and Co depletion. All values of Γ for APT results are plotted in Table 1.

The thickness of the GB region where segregation occurs is determined by analyzing 6 GBs by APT (3 from HP-1173K and 3 from HP-1373K) and has a value of 4.3 ± 0.8 nm. Therefore, a thickness of 4 nm is used to calculate f_{GB} in Eq. (4).

STEM-EDX and APT results confirm that Fe segregation and Co depletion are present in all studied GBs with comparable magnitude. We hypothesize that the Fe segregation at the GBs is responsible for the increase in the electrical conductivity at the GBs, having a measurable impact on bulk properties as shown in Fig. 2.

Substitutional Fe dopants on the Co sites act as acceptors in the material. By increasing the concentration of Fe dopants at the GBs, the local hole concentration is also enhanced and thus the electrical conductivity. We can think of the material as a composite of highly doped GB material with high conductivity and low Seebeck, and slightly less doped grain material with lower conductivity and higher Seebeck. Increasing the overall volume of GBs will lead to an increase in the conductivity, especially when the pathway of high conductivity material is uninterrupted. The Seebeck coefficient of a composite depends not only on the Seebeck coefficients of each material, but also the thermal conductivity of each material and what the proportional temperature drops across each material is. This makes calculating the Seebeck coefficient of a composite much more challenging than calculating the conductivity, especially in a brick layer model that has both parallel and series components to keep track of. In our data we see the material with more GBs has a lower Seebeck, which is not unexpected given that the small grained material would volumetrically have more highly doped lower Seebeck material in it than the larger grained sample.

3.4. Atomic arrangement at GBs

Besides chemical composition, it is known that the arrangement of the atoms at a GB can affect the properties of the material [61–63,27]. In order to study this phenomenon, atomic resolution STEM experiments are conducted to unravel the atomic structure of the GBs.

Fig. 4a shows a HAADF-STEM image of a high angle GB together with the fast Fourier transforms (FFTs) of both grains. The lower grain is aligned to the ⟨$\bar{1}$10⟩ zone axis while only one set of {111} planes is visible in the upper grain and the GB is parallel to the (111) plane of the lower grain. The EDX maps at the corresponding location confirms the Fe segregation and Co depletion. Γ values are −0.4 atoms nm^{-2} for Ti, 7.2 atoms nm^{-2} for Fe, −8.4 atoms nm^{-2} for Co and 1.6 atoms nm^{-2} for Sb. Therefore, this GB is a typical high angle GB with segregation comparable with the average values in Fig. 3c. The Sb site appears brighter due to the increased scattering amplitude of Sb while the Ti

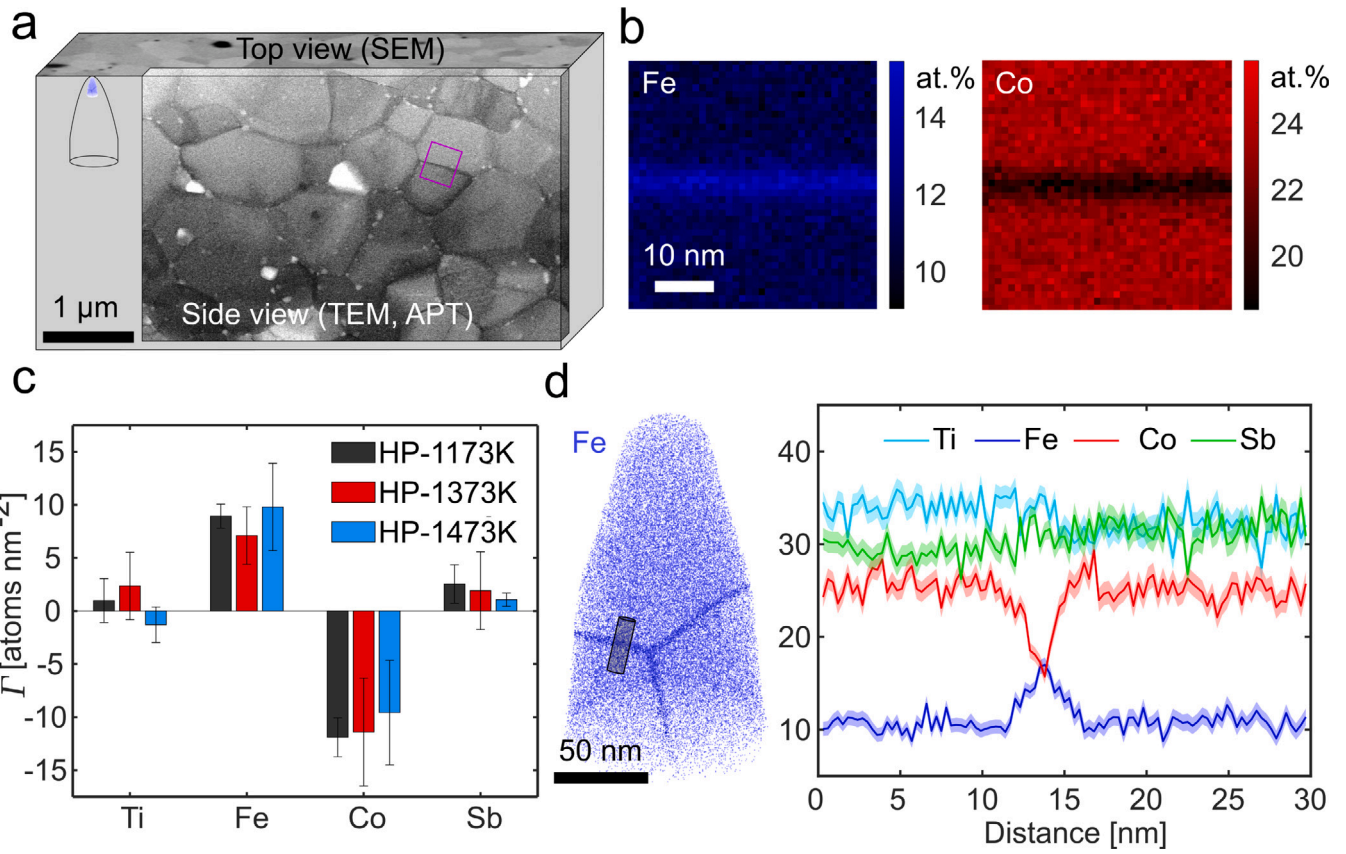

Fig. 3. (a) Scheme showing the scales of TEM and APT experiments with real pictures and approximate shapes and SEM image at the top (surface of the sample), (b) EDX at.% maps of a GB showing Fe segregation and Co depletion, (c) Γ from STEM-EDX data for HP-1173K, HP-1373K and HP-1473K and (d) APT reconstruction of HP-1373K for Fe showing a triple junction with segregation in the three GBs and a composition profile of the black cylinder area for Ti (light blue), Fe (dark blue), Co (red) and Sb (green) in at.%. (For interpretation of the references to color in this figure legend, the reader is referred to the web version of this article.)

site appears less bright alternating in intensity in a 1:1 sequence in the ⟨220⟩ direction.

Fig. 4b presents the HAADF-STEM image of a $\Sigma 3$ twin boundary, as evident from the FFTs of both grains. Both grains are aligned to the $\langle \bar{1}10 \rangle$ zone axis and the GB plane is the common (111) of both grains, confirming this is a coherent $\Sigma 3$ GB. An atomic representation is overlaid in the image, where the GB is a coherent mirror plane between the two grains. EDX maps do not indicate any segregation of Fe and Co. Therefore, we expect that coherent $\Sigma 3$ GBs do not contribute to the electrical conductivity enhancement. The absence of segregation at coherent $\Sigma 3$ GBs is an exception that can be explained by the low energy of this GB [64]. Since the distribution of GB misorientations is random for all studied samples (shown in Supplemental Fig. 2b), only a small fraction of the GBs are $\Sigma 3$ [65]. We note again that the calculated σ_{GB} is the average effect of all GBs on the bulk electrical conductivity.

No change in the atomic arrangement was found in most of the studied GBs compared to the grain interior. Thus, the unusual enhancement in the electrical conductivity for samples with higher fractions of GB phases is mainly attributed to the segregation of Fe and depletion of Co at GBs. Co and Fe share the 4b crystallographic position and have very similar atomic radius, 125 and 124 pm, respectively. Therefore, by modifying the ratio between Co and Fe on the 4b site, it is possible to change the chemical composition without changing the crystal structure. Nevertheless, we note that higher Fe doping (> 30%) would eventually decrease the zT of TiCoSb thermoelectrics [39], so that the observed GB phases would not be a good thermoelectric material in their bulk form. Nevertheless, we have demonstrated that by introducing them at GBs, the thermal conductivity can be reduced with simultaneous improvement on the electrical conductivity. For further designs of GBs to benefit overall zT, the Seebeck coefficient needs to be further decoupled from the carrier concentration, e.g. by using the carrier filtering effects [66,67]. We further note that the developed

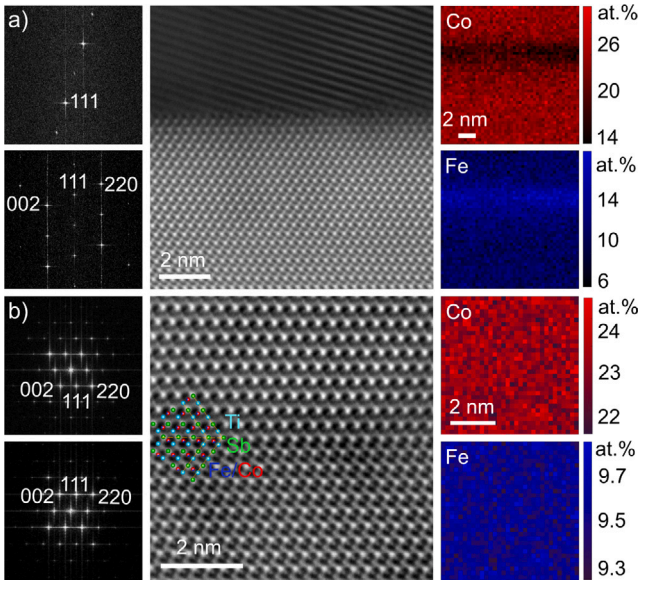

Fig. 4. HAADF-STEM images of (a) a high angle GB where the lower grain is along the $\langle \bar{1}10 \rangle$ zone axis, with the corresponding FFTs of both grains and EDX maps of Fe and Co, and (b) a coherent $\Sigma 3$ GB where both grains are along the $\langle \bar{1}10 \rangle$ zone axis, with atomic representations overlaid in the image, corresponding FFTs of both grains, and EDX maps of Fe and Co.

2-phase model can be applied to any material presenting electrically conductive GBs within less conductive grains, complementing to the 2-phase model introduced to treat electrically resistive GBs [15].

4. Conclusions

Our results demonstrate that $TiCo_{0.7}Fe_{0.3}Sb$ contains conductive GBs that increase the overall electrical conductivity while decreasing the thermal conductivity. The correlation between the electrical conductivity and the area fraction of GBs was demonstrated. Based on this observation, we developed a 2-phase model to calculate the contributions of the grain interior and GBs to the measured electrical conductivity. APT and STEM-EDX have shown that GBs contain Fe segregation and Co depletion of comparable magnitude across all GBs and samples with the exception of coherent $\Sigma 3$ GBs. HAADF-STEM revealed that most GBs do not have a special structural arrangement, while the enrichment of Fe dopants on Co sites would explain the more conductive behavior of GBs. GB segregation is a powerful tool to revert resistive fine-grained materials to be more conductive than their coarse-grained counterparts. For thermoelectrics, GB engineering presents a unique opportunity to simultaneously increase the electrical conductivity and decrease the thermal conductivity. We have demonstrated how detailed microstructure analysis can rationalize such design principles, which are being applied to more half-Heusler and other thermoelectrics [68,21]. At the same time, more efficient methods are also needed to screen for materials systems with favorable GB segregation, which have been mapped for binary alloys [34]. With increasing activity from high-throughput computational searches for thermoelectric materials [69,70], we propose that GB segregation is a promising area to calculate and design.

Declaration of competing interest

The authors declare that they have no known competing financial interests or personal relationships that could have appeared to influence the work reported in this paper.

Acknowledgments

The authors acknowledge Benjamin Breitbach for conducting the X-ray diffraction experiments.

Funding

R.B.V. acknowledges the support from the International Max Planck Research School for Interface Controlled Materials for Energy Conversion (IMPRS-SurMat). M.W.'s research at the Jet Propulsion Laboratory was supported by an appointment to the NASA Postdoctoral Program, administered by the Universities Space Research Association under contract with the NASA. T.L. acknowledges the financial support from the Alexander von Humboldt Foundation, Germany. G.J.S. acknowledges the support of award 70NANB19H005 from NIST as part of the Center for Hierarchical Materials Design (CHiMaD), United States. C.S. acknowledges funding from the German research foundation (DFG), Germany within the Collaborative Research Centre SFB 1394 "Structural and Chemical Atomic Complexity — From Defect Phase Diagrams to Materials Properties" (Project ID 409476157). S.Z. acknowledges funding from the DFG, Germany under the framework of SPP 2370 (Project number: 502202153).

Appendix A. Supplementary data

Supplementary material related to this article can be found online at https://doi.org/10.1016/j.actamat.2023.118816.

References

[1] S. LeBlanc, S.K. Yee, M.L. Scullin, C. Dames, K.E. Goodson, Material and manufacturing cost considerations for thermoelectrics, Renew. Sustain. Energy Rev. 32 (2014) 313–327, http://dx.doi.org/10.1016/j.rser.2013.12.030.

[2] J. Mao, G. Chen, Z. Ren, Thermoelectric cooling materials, Nature Mater. 20 (4) (2021) 454–461, http://dx.doi.org/10.1038/s41563-020-00852-w.

[3] A. Sood, R. Cheaito, T. Bai, H. Kwon, Y. Wang, C. Li, L. Yates, T. Bougher, S. Graham, M. Asheghi, M. Goorsky, K.E. Goodson, Direct visualization of thermal conductivity suppression due to enhanced phonon scattering near individual grain boundaries, Nano Lett. 18 (6) (2018) 3466–3472, http://dx.doi.org/10.1021/acs.nanolett.8b00534.

[4] H. Dong, B. Wen, R. Melnik, Relative importance of grain boundaries and size effects in thermal conductivity of nanocrystalline materials, Sci. Rep. 4 (1) (2014) 7037, http://dx.doi.org/10.1038/srep07037.

[5] P.G. Klemens, Phonon scattering and thermal resistance due to grain boundaries, Int. J. Thermophys. 15 (6) (1994) 1345–1351, http://dx.doi.org/10.1007/BF01458842.

[6] W.E. Taylor, N.H. Odell, H.Y. Fan, Grain boundary barriers in germanium, Phys. Rev. 88 (4) (1952) 867–875, http://dx.doi.org/10.1103/PhysRev.88.867.

[7] A.F. Mayadas, M. Shatzkes, Electrical-resistivity model for polycrystalline films: The case of arbitrary reflection at external surfaces, Phys. Rev. B 1 (4) (1970) 1382–1389, http://dx.doi.org/10.1103/PhysRevB.1.1382.

[8] J.Y.W. Seto, The electrical properties of polycrystalline silicon films, J. Appl. Phys. 46 (12) (1975) 5247–5254, http://dx.doi.org/10.1063/1.321593.

[9] G.E. Pike, C.H. Seager, The DC voltage dependence of semiconductor grain-boundary resistance, J. Appl. Phys. 50 (5) (1979) 3414–3422, http://dx.doi.org/10.1063/1.326334.

[10] F. Greuter, G. Blatter, Electrical properties of grain boundaries in polycrystalline compound semiconductors, Semicond. Sci. Technol. 5 (2) (1990) 111–137, http://dx.doi.org/10.1088/0268-1242/5/2/001.

[11] J. De Boor, T. Dasgupta, H. Kolb, C. Compere, K. Kelm, E. Mueller, Microstructural effects on thermoelectric efficiency: A case study on magnesium silicide, Acta Mater. 77 (2014) 68–75, http://dx.doi.org/10.1016/j.actamat.2014.05.041.

[12] S. Wang, S. Hui, K. Peng, T.P. Bailey, X. Zhou, X. Tang, C. Uher, Grain boundary scattering effects on mobilities in P-type polycrystalline SnSe, J. Mater. Chem. C 5 (39) (2017) 10191–10200, http://dx.doi.org/10.1039/C7TC03022C.

[13] J.-H. Son, M.-W. Oh, B.-S. Kim, S.-D. Park, Optimization of thermoelectric properties of N-type $Bi_2(Te, Se)_3$ with optimizing ball milling time, Rare Met. 37 (4) (2018) 351–359, http://dx.doi.org/10.1007/s12598-018-1028-8.

[14] K. Imasato, C. Fu, Y. Pan, M. Wood, J.J. Kuo, C. Felser, G.J. Snyder, Metallic N-type Mg_3Sb_2 single crystals demonstrate the absence of ionized impurity scattering and enhanced thermoelectric performance, Adv. Mater. 32 (16) (2020) 1908218, http://dx.doi.org/10.1002/adma.201908218.

[15] J.J. Kuo, M. Wood, T.J. Slade, M.G. Kanatzidis, G.J. Snyder, Systematic overestimation of lattice thermal conductivity in materials with electrically-resistive grain boundaries, Energy Environ. Sci. 13 (4) (2020) 1250–1258, http://dx.doi.org/10.1039/c9ee03921j.

[16] M. Wood, J.J. Kuo, K. Imasato, G.J. Snyder, Improvement of low-temperature zT in a Mg_3Sb_2–Mg_3Bi_2 solid solution via Mg-vapor annealing, Adv. Mater. 31 (35) (2019) 1902337, http://dx.doi.org/10.1002/adma.201902337.

[17] T.J. Slade, J.A. Grovogui, J.J. Kuo, S. Anand, T.P. Bailey, M. Wood, C. Uher, G.J. Snyder, V.P. Dravid, M.G. Kanatzidis, Understanding the thermally activated charge transport in NaPbmSbQm+2 (Q = S, Se, Te) thermoelectrics: Weak dielectric screening leads to grain boundary dominated charge carrier scattering, Energy Environ. Sci. 13 (5) (2020) 1509–1518, http://dx.doi.org/10.1039/D0EE00491J.

[18] Q. Qiu, Y. Liu, K. Xia, T. Fang, J. Yu, X. Zhao, T. Zhu, Grain boundary scattering of charge transport in N-type (Hf, Zr)CoSb half-Heusler thermoelectric materials, Adv. Energy Mater. 9 (11) (2019) 1803447, http://dx.doi.org/10.1002/aenm.201803447.

[19] M. César, D. Gall, H. Guo, Reducing grain-boundary resistivity of copper nanowires by doping, Phys. Rev. A 5 (5) (2016) 54018, http://dx.doi.org/10.1103/PhysRevApplied.5.054018.

[20] T. Luo, F. Serrano-Sánchez, H. Bishara, S. Zhang, B. Villoro, J.J. Kuo, C. Felser, C. Scheu, G.J. Snyder, J.P. Best, G. Dehm, Y. Yu, D. Raabe, C. Fu, B. Gault, Dopant-segregation to grain boundaries controls electrical conductivity of n-type NbCo(Pt)Sn half-Heusler alloy mediating thermoelectric performance, Acta Mater. 217 (2021) 117147, http://dx.doi.org/10.1016/j.actamat.2021.117147.

[21] R. Bueno Villoro, D. Zavanelli, C. Jung, D.A. Mattlat, R. Hatami Naderloo, N. Pérez Rodríguez, K. Nielsch, G.J. Snyder, C. Scheu, R. He, S. Zhang, Grain boundary phases in NbFeSb half-Heusler alloys: A new avenue to tune transport properties of thermoelectric materials, Adv. Energy Mater. 2204321 (2023) http://dx.doi.org/10.1002/aenm.202204321.

[22] J. Luo, Interfacial engineering of solid electrolytes, J. Materiomics 1 (1) (2015) 22–32, http://dx.doi.org/10.1016/j.jmat.2015.03.002.

[23] Y. Furushima, A. Nakamura, E. Tochigi, Y. Ikuhara, K. Toyoura, K. Matsunaga, Dislocation structures and electrical conduction properties of low angle tilt grain boundaries in $LiNbO_3$, J. Appl. Phys. 120 (14) (2016) 142107, http://dx.doi.org/10.1063/1.4961706.

[24] R.A. De Souza, J. Fleig, J. Maier, Z. Zhang, W. Sigle, M. Rühle, Electrical resistance of low-angle tilt grain boundaries in acceptor-doped $SrTiO_3$ as a function of misorientation angle, J. Appl. Phys. 97 (5) (2005) 53502, http://dx.doi.org/10.1063/1.1853495.

[25] T. Watanabe, Grain boundary engineering: Historical perspective and future prospects, J. Mater. Sci. 46 (12) (2011) 4095–4115, http://dx.doi.org/10.1007/s10853-011-5393-z.

[26] D. Raabe, M. Herbig, S. Sandlöbes, Y. Li, D. Tytko, M. Kuzmina, D. Ponge, P.-P. Choi, Grain boundary segregation engineering in metallic alloys: A pathway to the design of interfaces, Curr. Opin. Solid State Mater. Sci. 18 (4) (2014) 253–261, http://dx.doi.org/10.1016/j.cossms.2014.06.002.

[27] K. Lohani, H. Nautiyal, N. Ataollahi, K. Maji, E. Guilmeau, P. Scardi, Effects of grain size on the thermoelectric properties of Cu_2SnS_3: An experimental and first-principles study, ACS Appl. Energy Mater. (2021) http://dx.doi.org/10.1021/acsaem.1c02377.

[28] R.J. Quinn, J.-W.G. Bos, Advances in half-Heusler alloys for thermoelectric power generation, Mater. Adv. 2 (19) (2021) 6246–6266.

[29] D. Black, L. Schoensee, J. Richardson, T. Vleisides, N. Kempf, D. Wang, Z. Ren, Y. Zhang, Power generation from nanostructured half-Heusler thermoelectrics for efficient and robust energy harvesting, ACS Appl. Energy Mater. 1 (11) (2018) 5986–5992, http://dx.doi.org/10.1021/acsaem.8b01042.

[30] W. Li, A. Nozariasbmarz, R.A. Kishore, H.B. Kang, C. Dettor, H. Zhu, B. Poudel, S. Priya, Conformal high-power-density half-Heusler thermoelectric modules: A pathway toward practical power generators, ACS Appl. Mater. Interfaces 13 (45) (2021) 53935–53944, http://dx.doi.org/10.1021/acsami.1c16117.

[31] Y. Zhang, M. Cleary, X. Wang, N. Kempf, L. Schoensee, J. Yang, G. Joshi, L. Meda, High-temperature and high-power-density nanostructured thermoelectric generator for automotive waste heat recovery, Energy Convers. Manage. 105 (2015) 946–950, http://dx.doi.org/10.1016/j.enconman.2015.08.051.

[32] F. Casper, T. Graf, S. Chadov, B. Balke, C. Felser, Half-Heusler compounds: Novel materials for energy and spintronic applications, Semicond. Sci. Technol. 27 (6) (2012) 63001, http://dx.doi.org/10.1088/0268-1242/27/6/063001.

[33] C. Tongjai, H.A. Murdoch, C.A. Schuh, Design of stable nanocrystalline alloys, Science 337 (6097) (2012) 951–954, http://dx.doi.org/10.1126/science.1224737.

[34] H.A. Murdoch, C.A. Schuh, Estimation of grain boundary segregation enthalpy and its role in stable nanocrystalline alloy design, J. Mater. Res. 28 (16) (2013) 2154–2163, http://dx.doi.org/10.1557/jmr.2013.211.

[35] W. Xing, A.R. Kalidindi, D. Amram, C.A. Schuh, Solute interaction effects on grain boundary segregation in ternary alloys, Acta Mater. 161 (2018) 285–294, http://dx.doi.org/10.1016/j.actamat.2018.09.005.

[36] S.G. Kim, Y.B. Park, Grain boundary segregation, solute drag and abnormal grain growth, Acta Mater. 56 (15) (2008) 3739–3753, http://dx.doi.org/10.1016/j.actamat.2008.04.007.

[37] Z. Liu, N. Sato, W. Gao, K. Yubuta, N. Kawamoto, M. Mitome, K. Kurashima, Y. Owada, K. Nagase, C.-H. Lee, J. Yi, K. Tsuchiya, T. Mori, Demonstration of ultrahigh thermoelectric efficiency of ~7.3% in Mg_3Sb_2/MgAgSb module for low-temperature energy harvesting, Joule 5 (5) (2021) 1196–1208, http://dx.doi.org/10.1016/j.joule.2021.03.017.

[38] N. Naghibolashrafi, V.I. Hegde, K.C. Shambhu, S. Keshavarz, S.S. Naghavi, J. Ma, A. Gupta, P. LeClair, W.H. Butler, C. Wolverton, K. Munira, D. Mazumdar, A.W. Ghosh, Structural and magnetic analyses of the FexCo1-xTiSb alloy system: Fe0.5Co0.5TiSb as a prototypical half-Heusler compound, J. Alloys Compd. 822 (2020) 1–10, http://dx.doi.org/10.1016/j.jallcom.2019.153408.

[39] T. Wu, W. Jiang, X. Li, Y. Zhou, L. Chen, Thermoelectric properties of P-type Fe-doped TiCoSb half-Heusler compounds, J. Appl. Phys. 102 (10) (2007) 103705, http://dx.doi.org/10.1063/1.2809377.

[40] M. Schaffer, B. Schaffer, Q. Ramasse, Sample preparation for atomic-resolution STEM at low voltages by FIB, Ultramicroscopy 114 (2012) 62–71, http://dx.doi.org/10.1016/j.ultramic.2012.01.005.

[41] S. Zhang, C. Scheu, Evaluation of EELS spectrum imaging data by spectral components and factors from multivariate analysis, Microscopy 67 (suppl_1) (2018) i133–i141, http://dx.doi.org/10.1093/jmicro/dfx091.

[42] K. Thompson, D. Lawrence, D.J. Larson, J.D. Olson, T.F. Kelly, B. Gorman, In situ site-specific specimen preparation for atom probe tomography, Ultramicroscopy 107 (2) (2007) 131–139, http://dx.doi.org/10.1016/j.ultramic.2006.06.008.

[43] J.K. Mackenzie, Second paper on statistics associated with the random disorientation of cubes, Biometrika 45 (1–2) (1958) 229–240, http://dx.doi.org/10.1093/biomet/45.1-2.229.

[44] S. Zhang, Z. Xie, P. Keuter, S. Ahmad, L. Abdellaoui, X. Zhou, N. Cautaerts, B. Breitbach, S. Aliramaji, S. Korte-Kerzel, M. Hans, J.M. Schneider, C. Scheu, Atomistic structures of ⟨0001⟩ tilt grain boundaries in a textured Mg thin film, Nanoscale 14 (48) (2022) 18192–18199, http://dx.doi.org/10.1039/D2NR05505H.

[45] L. Abdellaoui, S. Zhang, S. Zaefferer, R. Bueno-Villoro, A. Baranovskiy, O. Cojocaru-Mirédin, Y. Yu, Y. Amouyal, D. Raabe, G.J. Snyder, C. Scheu, Density, distribution and nature of planar faults in silver antimony telluride for thermoelectric applications, Acta Mater. 178 (2019) 135–145, http://dx.doi.org/10.1016/j.actamat.2019.07.031.

[46] L. Abdellaoui, Z. Chen, Y. Yu, T. Luo, R. Hanus, T. Schwarz, R. Bueno Villoro, O. Cojocaru-Mirédin, G.J. Snyder, D. Raabe, Y. Pei, C. Scheu, S. Zhang, Parallel dislocation networks and cottrell atmospheres reduce thermal conductivity of PbTe thermoelectrics, Adv. Funct. Mater. 31 (20) (2021) 2101214, http://dx.doi.org/10.1002/adfm.202101214.

[47] H. Bishara, S. Lee, T. Brink, M. Ghidelli, G. Dehm, Understanding grain boundary electrical resistivity in Cu: The effect of boundary structure, ACS Nano 15 (10) (2021) 16607–16615, http://dx.doi.org/10.1021/acsnano.1c06367.

[48] M.H. Enayati, F.A. Mohamed, Application of mechanical alloying/milling for synthesis of nanocrystalline and amorphous materials, Int. Mater. Rev. 59 (7) (2014) 394–416, http://dx.doi.org/10.1179/1743280414Y.0000000036.

[49] L.J. van der Pauw, A method of measuring specific resistivity and Hall effect of discs of arbitrary shape, Philips Res. Rep. 13 (1) (1958) 1–9.

[50] G.J. Snyder, A. Pereyra, R. Gurunathan, Effective mass from seebeck coefficient, Adv. Funct. Mater. 32 (20) (2022) 2112772, http://dx.doi.org/10.1002/adfm.202112772.

[51] K.H. Lee, S.-i. Kim, J.-C. Lim, J.Y. Cho, H. Yang, H.-S. Kim, Approach to determine the density-of-states effective mass with carrier concentration-dependent seebeck coefficient, Adv. Funct. Mater. 32 (33) (2022) 2203852, http://dx.doi.org/10.1002/adfm.202203852.

[52] G.J. Snyder, A.H. Snyder, M. Wood, R. Gurunathan, B.H. Snyder, C. Niu, Weighted mobility, Adv. Mater. 32 (25) (2020) 2001537, http://dx.doi.org/10.1002/adma.202001537.

[53] C. Hu, K. Xia, C. Fu, X. Zhao, T. Zhu, Carrier grain boundary scattering in thermoelectric materials, Energy Environ. Sci. 15 (4) (2022) 1406–1422, http://dx.doi.org/10.1039/D1EE03802H.

[54] H.-S. Kim, Z.M. Gibbs, Y. Tang, H. Wang, G.J. Snyder, Characterization of Lorenz number with seebeck coefficient measurement, APL Mater. 3 (4) (2015) 41506, http://dx.doi.org/10.1063/1.4908244.

[55] D.M. Rowe, V.S. Shukla, N. Savvides, Phonon scattering at grain boundaries in heavily doped fine-grained silicon–germanium alloys, Nature 290 (5809) (1981) 765–766, http://dx.doi.org/10.1038/290765a0.

[56] X.W. Wang, H. Lee, Y.C. Lan, G.H. Zhu, G. Joshi, D.Z. Wang, J. Yang, A.J. Muto, M.Y. Tang, J. Klatsky, S. Song, M.S. Dresselhaus, G. Chen, Z.F. Ren, Enhanced thermoelectric figure of merit in nanostructured N-type silicon germanium bulk alloy, Appl. Phys. Lett. 93 (19) (2008) 193121, http://dx.doi.org/10.1063/1.3027060.

[57] P.G. Klemens, Thermal conductivity and lattice vibrational modes, in: F. Seitz, D. Turnbull (Eds.), Solid State Physics, vol. 7, Academic Press, 1958, pp. 1–98, http://dx.doi.org/10.1016/S0081-1947(08)60551-2.

[58] Y. Yu, C. Zhou, S. Zhang, M. Zhu, M. Wuttig, C. Scheu, D. Raabe, G.J. Snyder, B. Gault, O. Cojocaru-Mirédin, Revealing nano-chemistry at lattice defects in thermoelectric materials using atom probe tomography, Mater. Today 32 (2020) 260–274, http://dx.doi.org/10.1016/j.mattod.2019.11.010.

[59] B.W. Krakauer, D.N. Seidman, Absolute atomic-scale measurements of the Gibbsian interfacial excess of solute at internal interfaces, Phys. Rev. B 48 (9) (1993) 6724–6727, http://dx.doi.org/10.1103/PhysRevB.48.6724.

[60] P. Maugis, K. Hoummada, A methodology for the measurement of the interfacial excess of solute at a grain boundary, Scr. Mater. 120 (2016) 90–93, http://dx.doi.org/10.1016/j.scriptamat.2016.04.005.

[61] P.R. Cantwell, M. Tang, S.J. Dillon, J. Luo, G.S. Rohrer, M.P. Harmer, Grain boundary complexions, Acta Mater. 62 (1) (2014) 1–48, http://dx.doi.org/10.1016/j.actamat.2013.07.037.

[62] Y. Sato, T. Yamamoto, Y. Ikuhara, Atomic structures and electrical properties of ZnO grain boundaries, J. Am. Ceram. Soc. 90 (2) (2007) 337–357, http://dx.doi.org/10.1111/j.1551-2916.2006.01481.x.

[63] M.G. Tsoutsouva, P.E. Vullum, K. Adamczyk, M. Di Sabatino, G. Stokkan, Interfacial atomic structure and electrical activity of nano-facetted CSL grain boundaries in high-performance multi-crystalline silicon, J. Appl. Phys. 127 (12) (2020) 125109, http://dx.doi.org/10.1063/1.5130996.

[64] M. Herbig, D. Raabe, Y.J. Li, P. Choi, S. Zaefferer, S. Goto, Atomic-scale quantification of grain boundary segregation in nanocrystalline material, Phys. Rev. Lett. 112 (12) (2014) 126103, http://dx.doi.org/10.1103/PhysRevLett.112.126103.

[65] A. Morawiec, J.A. Szpunar, D.C. Hinz, Texture influence on the frequency of occurrence of CSL-boundaries in polycrystalline materials, Acta Metall. Mater. 41 (10) (1993) 2825–2832, http://dx.doi.org/10.1016/0956-7151(93)90097-C.

[66] A. Soni, Y. Shen, M. Yin, Y. Zhao, L. Yu, X. Hu, Z. Dong, K.A. Khor, M.S. Dresselhaus, Q. Xiong, Interface driven energy filtering of thermoelectric power in spark plasma sintered Bi_2Te_2.7Se0.3 nanoplatelet composites, Nano Lett. 12 (8) (2012) 4305–4310, http://dx.doi.org/10.1021/nl302017w.

[67] C. Gayner, Y. Amouyal, Energy filtering of charge carriers: Current trends, challenges, and prospects for thermoelectric materials, Adv. Funct. Mater. 30 (18) (2020) 1901789, http://dx.doi.org/10.1002/adfm.201901789.

[68] C. Zhang, G. Yan, Y. Wang, X. Wu, L. Hu, F. Liu, W. Ao, O. Cojocaru-Mirédin, M. Wuttig, G.J. Snyder, Y. Yu, Grain boundary complexions enable a simultaneous optimization of electron and phonon transport leading to high-performance GeTe thermoelectric devices, Adv. Energy Mater. (2022) 2203361, http://dx.doi.org/10.1002/aenm.202203361.

[69] P. Gorai, V. Stevanović, E.S. Toberer, Computationally guided discovery of thermoelectric materials, Nat. Rev. Mater. 2 (9) (2017) 1–16, http://dx.doi.org/10.1038/natrevmats.2017.53.

[70] J. Carrete, N. Mingo, S. Wang, S. Curtarolo, Nanograined half-Heusler semiconductors as advanced thermoelectrics: An Ab initio high-throughput statistical study, Adv. Funct. Mater. 24 (47) (2014) 7427–7432, http://dx.doi.org/10.1002/adfm.201401201.